

A Self-Consistent Hubble Expansion in $f(T)$ Gravity model: Confrontation with Recent Observations

*K. Sri Kavya*¹, *T. Vinutha*², and *B. Revathi*²

¹Department of Science and Humanities, MVGR College of Engineering, India.

²Department of Applied Mathematics, Andhra University, Visakhapatnam, India.

kavyasriaparna@gmail.com

vinuthatummal@gmail.com

bandaru.revathi19@gmail.com

Abstract

The accelerated expansion of the universe remains one of the most profound puzzles in modern cosmology, often attributed to dark energy within the framework of General Relativity. As an alternative, modified teleparallel gravity theories such as $f(T)$ gravity offer a purely geometric mechanism to explain cosmic acceleration. In this work, we construct a plane-symmetric anisotropic cosmological model in the framework of exponential $f(T)$ gravity, adopting the functional form $f(T) = T + ue^{-vT}$. A key novelty of this study is that the Hubble function $H(z)$ is derived self-consistently from the field equations rather than being prescribed phenomenologically. Furthermore, we provide the first comprehensive observational test of an anisotropic $f(T)$ model using a combination of DESI, gravitational-wave (GW) data, and complementary datasets including OHD, CMB, and Pantheon+SH0ES. Our best-fit analysis yields $70 \lesssim H_0 \lesssim 73 \text{ km s}^{-1} \text{ Mpc}^{-1}$, $0.28 \lesssim \Omega_m \lesssim 0.34$, and $-0.99 \lesssim \omega \lesssim -0.69$, all consistent with current late-time cosmological observations. The model accurately reproduces the distance modulus of Type Ia supernovae and the luminosity-distance relation from gravitational-wave standard sirens. These results demonstrate that the proposed anisotropic exponential $f(T)$ model can account for the observed cosmic acceleration without invoking a dark-energy component, thereby offering a novel and observationally consistent framework for studying anisotropic extensions of gravity.

Key words: Plane Symmetric anisotropic cosmological model, Modified theory, Perfect fluid.

1 Introduction

The expansion of the universe has remained an intriguing research topic in recent decades, but several astronomers have elucidated that the universe comprises two fundamental constituents: namely, dark matter and dark energy. These enigmatic entities play a pivotal role in shaping the cosmos and driving its perpetual expansion. Two eminent research teams [1, 2] have concluded that dark energy plays a pivotal role in the study of the universe's accelerated expansion. Moreover, various observational

datasets have furnished indirect yet compelling evidence of this cosmic acceleration. There are several theories to describe this cosmic acceleration, one of them is Teleparallel Gravity (TG) [3], which is equivalent to General Relativity (GR).

Teleparallel Gravity (TG) is a dynamically equivalent reformulation of General Relativity (GR), wherein gravity is attributed to torsion rather than spacetime curvature. It was originally introduced by Einstein as part of his attempt to unify electromagnetism with gravity, offering an alternative geometric description of the gravitational interaction. Unlike GR, which is formulated as a purely geometric theory based on curved spacetime, TG relies on a flat spacetime with torsion. More specifically, TG is framed as a gauge theory for the translation group, reflecting a fundamentally different mathematical structure. Despite these foundational differences, both TG and GR lead to identical field equations, that is why TG is often referred to as the Teleparallel Equivalent of General Relativity (TEGR) [4].

One of the most conceptually elegant and mathematically consistent generalisations of the TEGR is $f(T)$ gravity, wherein the torsion scalar T in the gravitational action is promoted to an arbitrary differentiable function $f(T)$. This modification parallels the structure of $f(R)$ gravity, a widely studied extension of General Relativity, where the Ricci scalar R is replaced by a general function $f(R)$ in the Einstein-Hilbert action, enabling a broader phenomenological framework and offering possible explanations for the late-time acceleration of the universe. Teleparallel dark energy models, involving non-minimal scalar-torsion coupling, offer alternatives to quintessence in explaining late-time acceleration [5, 6]. Additionally, non-local $f(T)$ gravity introduces inverse differential operators, inspired by quantum gravity, to improve the theory's ultraviolet behaviour [7]. Together, these generalizations expand the theoretical robustness and observational relevance of the teleparallel framework.

Motivated by the intrinsic elegance and analytical tractability of $f(T)$ gravity, we embark on an exploration within a generalized teleparallel framework, wherein the torsion scalar T in the Teleparallel Equivalent of General Relativity (TEGR) action is elevated to a smooth, differentiable function $f(T)$. This generalization preserves the second-order structure of the resulting field equations, unlike the fourth-order equations characterized in $f(R)$ gravity, thereby rendering the theory both theoretically compelling and computationally efficient. In this investigation, we adopt the conventional action for $f(T)$ gravity, expressed as:

$$S = \frac{1}{16\pi G} \int f(T) |e| d^4x + \int L_m |e| d^4x, \quad (1)$$

where G denotes the gravitational constant, and $|e|$ denotes the absolute value of the determinant of the tetrad (e_i^A). The term L_m corresponds to the matter Lagrangian density. For analytical convenience, the general function $f(T)$ is often written in the form

$$f(T) = T + F(T), \quad (2)$$

where T is the torsion scalar and $F(T)$ encodes deviations from the teleparallel equivalent of general relativity (TEGR). In $f(T)$ gravity, the torsion scalar is defined by

$$T = T^\gamma_{ij} S^{ij}_\gamma, \quad (3)$$

where T^γ_{ij} and S^{ij}_γ denote the torsion tensor and the superpotential respectively. The torsion tensor is given by

$$T^\gamma_{ij} = e^\gamma_A (\partial_i e^A_j - \partial_j e^A_i), \quad (4)$$

while the superpotential takes the form

$$S^{ij}_\gamma = \frac{1}{2} (K^{ij}_\gamma + \delta^i_\gamma T^{\alpha j}{}_\alpha - \delta^j_\gamma T^{\alpha i}{}_\alpha). \quad (5)$$

Here, K^{ij}_γ is the contorsion tensor, defined by

$$K^{ij}_\gamma = \frac{1}{2} (T^{ji}_\gamma + T_\gamma^{ij} - T^{ij}_\gamma). \quad (6)$$

Varying the action (1) with respect to the e_i^A yields the field equations in $f(T)$ gravity as

$$\left. \begin{aligned} e^{-1} \partial_i (e e^\gamma_A S_\gamma^{ij}) (1 + f_T) - e^\lambda_A T^\gamma_{i\lambda} S_\gamma^{ji} (1 + f_T) + e^\gamma_A S_\gamma^{ij} \partial_i T f_{TT} \\ - \frac{1}{4} e^j_A (T + f(T)) = 4\pi G e^\gamma_A T_\gamma^j. \end{aligned} \right\} \quad (7)$$

Within this framework, f_T and f_{TT} correspond to the first and second order functional derivatives of $f(T)$ with respect to the torsion scalar respectively. T_γ^j denotes the stress-energy–momentum tensor derived from the matter field Lagrangian.

Several authors have investigated this modified teleparallel framework in a wide range of contexts within cosmology and gravitational physics. In particular, $f(T)$ models have been employed to account for late-time cosmic acceleration without the need for a cosmological constant, and in many cases they can effectively mimic quintessence–like behaviour [3, 8]. A number of specific functional choices, including power–law and exponential deformations of the torsion scalar, have been confronted with observations from type Ia supernovae, baryon acoustic oscillations, cosmic microwave background data, and cosmic chronometers [9, 10]. Beyond background expansion, the theory has also been applied to astrophysical settings: it has been tested through lensing phenomena such as strongly lensed fast radio bursts, which provide promising new probes [11], and through solar–system dynamics where corrections appear in planetary orbits and light deflection [12]. In the early universe, torsion–based corrections have been considered in quantum cosmology and inflationary scenarios, with recent studies constructing inflation purely from torsional degrees of freedom or their non–local generalisations [13, 14]. On the theoretical side, important work has clarified issues of mathematical consistency, including Bianchi identities and local Lorentz invariance [15], while generalisations such as $f(T, B)$ gravity, where a boundary term bridges the torsion and curvature formalisms, have been

studied in homogeneous and isotropic cosmologies [16]. Altogether, these developments underline the versatility of $f(T)$ gravity as a candidate framework for addressing problems across cosmology, astrophysics, and the foundations of gravitational theory. Motivated by the aforementioned studies, in this work we consider a specific modification of teleparallel gravity described by the function

$$f(T) = T + \mu e^{-\nu T}, \quad (8)$$

where u and v denote arbitrary constants characterizing the deviation from the teleparallel equivalent of general relativity.

Anisotropy refers to the direction-dependence of physical properties in space or matter. In cosmology, an anisotropic universe expands at different rates along distinct spatial directions, in contrast to the isotropic case where the expansion is uniform. Observationally, anisotropy manifests through temperature fluctuations in the Cosmic Microwave Background (CMB), hemispherical power asymmetry, and preferred directional patterns in the large-scale structure of the Universe. Investigating such features provides critical tests of the cosmological principle of large-scale isotropy and places constraints on models of the early universe, inflationary scenarios, and possible deviations from the standard Λ CDM cosmology.

Despite extensive studies, most investigations of $f(T)$ gravity have been confined to isotropic and homogeneous Friedmann–Lemaître–Robertson–Walker (FLRW) geometries. However, several recent observations, including CMB hemispherical asymmetry and large-scale dipole anisotropies [17], suggest that mild deviations from isotropy may exist on cosmological scales. These findings have motivated renewed interest in anisotropic cosmological models as potential extensions of the standard Λ CDM paradigm. In particular, plane-symmetric space-times offer a mathematically tractable framework to investigate direction-dependent expansion rates and the isotropization process at late times. Several authors have carried out detailed studies of anisotropic cosmological models in different contexts, including Akarsu et al. [18], Vinutha et al. [19], Vinutha and Kavya [20], Koivisto and Mota [21], Shahc [22] and Rodrigues et al. [23], among others.

In the present work, we investigate a plane-symmetric anisotropic cosmological model within the framework of $f(T)$ gravity. For the functional form of the Lagrangian, we consider an exponential extension of the torsion scalar, expressed as $f(T) = T + \mu e^{-\nu T}$, where μ and ν are arbitrary model parameters. This choice is motivated by its ability to generalize the Teleparallel Equivalent of General Relativity (TEGR), since the standard linear form $f(T) = T$ is recovered in the limit $\mu = 0$. Exponential models of this type have been demonstrated to yield viable cosmological dynamics, including late-time accelerated expansion, and are therefore of considerable interest for studying anisotropic universes. In particular, their application to plane-symmetric spacetimes enables us to explore the direction-dependent influence of torsion on cosmic evolution, extending the analysis beyond the conventional isotropic framework. The structure of the paper is organized as follows. In Section 2, we

present the plane-symmetric metric and derive the corresponding field equations within the exponential $f(T)$ framework. Section 3 describes the observational datasets and the statistical methodology adopted for parameter estimation. The analysis and discussion of results are provided in Section 3.1, while Section 4 summarizes the main findings and conclusions of the study.

2 Model and field equations

The discovery of the universe's accelerated expansion has significantly redefined modern cosmology, introducing dark energy as a dominant yet elusive component of the cosmic framework. Although the standard Λ CDM model presumes large-scale isotropy and homogeneity, there exists no compelling theoretical or observational justification to assert that these conditions persisted throughout the entirety of cosmic history. Indeed, observations from Type Ia supernovae, the Cosmic Microwave Background (CMB), and large-scale structure indicate that the universe may have undergone anisotropic phases, especially during its early evolutionary stages. This motivates the exploration of anisotropic cosmological models, which provide a natural generalisation of the FLRW framework by incorporating directional dependence in the cosmic expansion dynamics. Such models gain particular relevance when coupled with dynamical dark energy components, such as scalar fields, as they facilitate a more comprehensive understanding of cosmic acceleration, structure formation, and potential departures from the cosmological principle. Consequently, the investigation of anisotropic cosmologies incorporating dark energy is both theoretically well-founded and observationally significant. By inspiring this in this article, we consider a time-dependent, plane-symmetric anisotropic spacetime of the form

$$(ds)^2 = e^{2h}(dt)^2 - e^{2h} [(dr)^2 + r^2(d\theta)^2 + s^2(dz)^2], \quad (9)$$

where h, s are function of time (t) only. Several researchers have worked with this metric across various domains of cosmology. Specifically, Mishra [24], Aditya et al. [25], Shamir and Saeed [26] and Rao and Vinutha [27] have analyzed a range of cosmological models within the framework of different theories of gravity.

The vierbein associated with the above metric is $e_i^A = \text{diag}(e^h, e^h, r e^h, s e^h)$, using this vierbein, the torsion of equation (9) is

$$T = \frac{-2\dot{h}}{e^{2h}} \left(3\dot{h} + \frac{2\dot{s}}{s} \right). \quad (10)$$

Moreover, in the present work, we consider the stress–energy–momentum tensor is taken to represent a perfect fluid, given by

$$\mathbf{T}_\gamma^{\mathbf{j}} = (1, \omega_r, \omega_\theta, \omega_z)\rho = (1, \omega + \alpha, \omega + \beta, \omega)\rho. \quad (11)$$

Along the r, θ and z axes, the directional equation of state ($\omega = \frac{p}{\rho}$) parameters are specified as $\omega_r = \omega + \alpha$, $\omega_\theta = \omega + \beta$ and $\omega_z = \omega$. Here, α and β serve as the skewness parameters, representing

the deviation from ω in the r, θ directions respectively. With the aid of equations (5) to (7), (10) and (11), the $f(T)$ field equations for the metric (9) are obtained as

$$f(T) + \frac{2f_T}{e^{2h}} \left[2\ddot{h} + \frac{\ddot{s}}{s} + 4\dot{h}^2 + \frac{4\dot{h}\dot{s}}{s} \right] + \frac{2f_{TT}\dot{T}}{e^{2h}} \left[2\dot{h} + \frac{\dot{s}}{s} \right] = -16\pi(\omega + \alpha)\rho, \quad (12)$$

$$f(T) + \frac{2f_T}{e^{2h}} \left[2\ddot{h} + \frac{\ddot{s}}{s} + 4\dot{h}^2 + \frac{4\dot{h}\dot{s}}{s} \right] + \frac{2f_{TT}\dot{T}}{e^{2h}} \left[2\dot{h} + \frac{\dot{s}}{s} \right] = -16\pi(\omega + \beta)\rho, \quad (13)$$

$$f(T) + \frac{4f_T}{e^{2h}} \left[\ddot{h} + 2\dot{h}^2 + \frac{\dot{h}\dot{s}}{s} \right] + \frac{4f_{TT}\dot{T}}{e^{2h}} \dot{h} = -16\pi\omega\rho, \quad (14)$$

$$f(T) + \frac{2f_T}{e^{2h}} \left[6\dot{h}^2 + 4\frac{\dot{h}\dot{s}}{s} \right] = 16\pi\rho. \quad (15)$$

From equation (12) and (13), it is clear that $\alpha = \beta$ and from equations (12) to (13) that the system is overdetermined. Since the number of unknown variables exceeds the number of independent equations, we impose two physically justified constraints to render the system which are both mathematically consistent and physically viable,

1) A detailed interpretation of this relation was articulated, and its fundamental significance was emphasised by Thorne [28]. Furthermore, the observational analyses of Kantowski and Sachs [29] and Kristian and Sachs [30] revealed that, at the present epoch, the Hubble expansion is isotropic to within approximately 30%. According to Collins et al. [31], in spatially homogeneous cosmological models, the shear scalar (σ) and the expansion scalar (θ) are fundamentally linked, with their ratio (σ/H) remaining invariant throughout cosmic evolution. This condition offers a natural mechanism to regulate anisotropy in such models and ensures compatibility with observational constraints, which suggest that the present cosmic expansion is nearly isotropic, with $\sigma/H \lesssim 0.3$. Motivated by this key insight, and in order to incorporate the interplay between anisotropy and expansion into our framework, we adopt the relation

$$e^h = s^\iota, \quad (16)$$

where $\iota \neq 1$ is an arbitrary constant. This relation effectively encapsulates the dynamical link between the shear scalar and the expansion scalar in our model.

2) In cosmology, the skewness parameter is introduced to quantify deviations from isotropy in cosmic pressure. While the standard FLRW model assumes isotropic pressure, anisotropic space-times such as Bianchi or Kantowski–Sachs allow directional variations in pressure. The skewness parameter modifies the equation of state to capture these anisotropic stresses, making it a valuable tool for probing anisotropic dark energy models and departures from the isotropic Λ CDM cosmology. Within the framework of $f(T)$ gravity, it further characterizes the impact of torsion-based modifications on anisotropy, enabling the study of how directional pressures influence cosmic expansion

and offering possible alternatives to explain late-time acceleration. The utility of this parameter has been highlighted in various works, particularly by Akarsu [32], Sharif and Zubair [33] and Divya and Aditya [34]. Motivated by these contributions, and in order to obtain exact solutions for the metric potentials in our framework, the relation between $\alpha(t)$ and ρ is assumed in the following form

$$\alpha(t) = -\frac{2\dot{s}f_T}{\omega e^{2h}s} \left(\alpha_0 - \frac{Tf_{TT}}{f_T} \right). \quad (17)$$

Using Equations (7), (8) and (12) to (17), we obtain the explicit forms of the metric potentials, which govern the anisotropic dynamics of the considered space-time model.

$$h = \log \left((\iota + 2) \left(\frac{e^{c\alpha_0 t}}{\alpha_0} + c_1 \right) \right)^{\frac{\iota}{\iota+2}}, \quad (18)$$

$$s = \left((\iota + 2) \left(\frac{e^{c\alpha_0 t}}{\alpha_0} + c_1 \right) \right)^{\frac{1}{\iota+2}}. \quad (19)$$

Using equations (12) to (14) and (18) and (19) the hubble parameter of the present anisotropic model is

$$H = \alpha_1 \left(\left(\frac{f(T)}{8} - 6\pi\omega\Omega_m H_0^2 \right) - \alpha_2\alpha_3 + \alpha_4 \right) \quad (20)$$

where

$$\begin{aligned} \alpha_1 &= -(\iota + 2)^7 \left(\frac{(1+z)^{\frac{-(3\iota+2)}{2\iota+1}} - c_1(\iota + 2)}{32\iota^5 c^7 \alpha_0^7 (3\iota + 2)^2} \right) \\ \alpha_2 &= \frac{-0.0416(\iota + 2)^4 \left((1+z)^{\frac{-(3\iota+2)}{2\iota+1}} - c_1(\iota + 2) \right)^{\frac{2}{\iota+2}}}{\iota^3 c^4 \alpha_0^4 (3\iota + 2)} \\ \alpha_3 &= \frac{c^2 \alpha_0^2 (2\iota^2 + 3\iota + 1)}{(\iota + 2)^2} \\ \alpha_4 &= \frac{\alpha_0 c \iota}{3\alpha_1(\iota + 2)} \\ f(T) &= \frac{1}{(\iota + 2)^2} \left[l(\iota + 2)^2 e^{\frac{6\iota c^2 \alpha_0 v \left(l + \frac{2}{3} \right) \left((1+z)^{\frac{-(3\iota+2)}{2\iota+1}} - c_1(\iota + 2) \right)^{\frac{-2\iota}{\iota+2}}}{(\iota + 2)^2}} \right. \\ &\quad \left. - 6\alpha_0^2 c^2 \iota \left(l + \frac{2}{3} \right) \left((1+z)^{\frac{-(3\iota+2)}{2\iota+1}} - c_1(\iota + 2) \right)^{\frac{-2\iota}{\iota+2}} \right] \end{aligned}$$

Owing to the highly nonlinear nature of the Hubble parameter, we adopt a Taylor series expansion in terms of redshift. For analytical convenience, higher-order contributions are neglected, yielding a simplified yet sufficiently accurate expression for practical cosmological analysis. Thus, the Hubble parameter can be expressed as

$$H = \left(\kappa_1 z^2 + \kappa_2 z + \kappa_3 \right) \Omega_m \omega H_0^2 + \kappa_4 \quad (21)$$

where $\kappa_1, \kappa_2, \kappa_3$ and κ_4 are arbitrary constants, and the detailed expressions are provided in the Appendix.

3 Observational Data and Methodological Framework

In this section, we present a comprehensive description of the observational data sets employed in the present analysis. The discussion highlights the sources, nature, and significance of the data, ensuring clarity regarding their role in constraining the model parameters. Particular emphasis is placed on the relevance of these data sets for testing the theoretical framework and establishing consistency with current cosmological observations.

Observational Hubble Data (OHD)

Direct measurements of the Hubble parameter $H(z)$ are provided by Observational Hubble Data (OHD), which play a pivotal role in reconstructing the universe's expansion dynamics. In this work, we employ a compilation of 33 OHD measurements spanning the redshift range $0.07 < z < 2.36$. Among these, 31 data points are derived using the cosmic chronometer(CC) method, which estimates the hubble parameter by analyzing the oldest passively evolving galaxies situated at close redshifts. This technique, often known as the differential age method, infers $H(z)$ from the age differences of such galaxies across various redshift intervals. Jimenez et al. [35] were the first to apply the CC approach, which was subsequently refined by Stern et al. [36] through red-envelope galaxies. Significant improvements were achieved by Moresco et al. [37] who obtained 5–12% precision in $H(z)$ measurements up to $z \approx 1.1$. Further contributions came from Zhang et al. [38] employing SDSS luminous red galaxies, and from Ratsimbazafy et al. [39], who extended the measurements to higher redshifts. More recently, Moresco et al. [40] presented 15 correlated CC data points, further strengthening the dataset. Beyond the CC sample, two additional high-redshift measurements at $z = 2.34$ and $z = 2.36$ are derived from baryon acoustic oscillation (BAO) signatures in the Ly- α forest [41], cross-correlated with quasistellar object (QSO) data. Collectively, this dataset provides a robust and model-independent probe of cosmic expansion across a broad redshift range. The chi-squared statistic corresponding to the 33 $H(z)$ measurements is defined as

$$\chi_{cc+Ly\alpha}^2 = \sum_{k=1}^{33} \frac{(H^{obs}(z_k) - H(z_k^{th}))^2}{\sigma_{H^{obs}(z_k)}^2}. \quad (22)$$

The symbol $H^{obs}(z_k)$ is used to designate the observationally derived Hubble parameter at the redshift(z_k), accompanied by the variance of its measurement uncertainty $\sigma_{H^{obs}(z_k)}^2$.

BAO

Baryon Acoustic Oscillations(BAO) arise as relic imprints of primordial sound waves propagating through the photon–baryon plasma of the early universe, manifesting today as a preferred clustering scale in the large-scale distribution of galaxies. Serving as a cosmological “standard ruler,” BAO provide precise measurements of cosmic distances and impose stringent constraints on the expansion history of the universe. By complementing supernovae and cosmic chronometers, BAO play a pivotal role in constraining the properties of dark energy and testing possible extensions of the standard Λ CDM framework. In particular, BAO observations are instrumental for probing both the angular diameter distance as a function of redshift and the redshift dependence of the Hubble parameter. These measurements are commonly expressed in terms of the dimensionless ratio

$$d(z) = \frac{r_s(z_d)}{D_V(z)}, \quad (23)$$

where $r_s(z_d)$ denotes the sound horizon at the drag epoch and is given by

$$r_s(z_d) = \int_{z_d}^{\infty} \frac{c_s dz}{H(z)}, \quad (24)$$

with c_s being the sound speed of the photon–baryon fluid and the volume-averaged distance $D_V(z)$, which links the line-of-sight(via $H(z)$) and transverse(via $D_A(z)$) clustering scales, is defined as

$$D_V(z) = \left((1+z)^2 D_A^2(z) \frac{cz}{H(z)} \right)^{\frac{1}{3}}, \quad (25)$$

where the angular diameter distance is

$$D_A(z) = \frac{c}{1+z} \int_0^z \frac{dz'}{H(z')}. \quad (26)$$

In this work, we use the latest DESI (Dark Energy Spectroscopic Instrument) data, including DR1 and the newly released DR2 Cosmology Results. DR2 provides updated Lyman-alpha and galaxy BAO measurements from observations conducted between May 2021 and April 2024, building on the extensive DR1 dataset, which contains spectra and redshifts for over 18 million celestial objects and the largest 3D map of the universe to date [42], along with eight BAO measurements obtained from 6dFGS [43], MGS [44], BOSS LOWZ [45], SDSS(R) [46], BOSS CMASS [45], and WiggleZ [47].

CMB

The Cosmic Microwave Background(CMB) is the relic radiation from the epoch of recombination ($z \approx 1100$), providing a snapshot of the early universe. It carries vital information about the geometry, composition, and expansion history of the cosmos. CMB observations, particularly through distance priors such as the acoustic scale l_a , defined as

$$l_a = \pi \frac{r(z_*)}{r_s(z_*)}, \quad (27)$$

play a crucial role in cosmological parameter estimation. The quantity $r(z_*)$ represents the comoving distance to the last scattering surface, expressed as

$$r(z_*) = \int_0^{z_*} \frac{cdz}{H(z)}. \quad (28)$$

Likewise, $r_s(z_*)$ characterizes the comoving sound horizon at recombination (see Eq. 24). Together with the decoupling redshift (z_*), these quantities provide a powerful set of diagnostics for testing cosmological models. From Planck 2015 data [48], the acoustic scale is reported as $l_a = 301.77 \pm 0.09$ evaluated at the redshift of last scattering $z_* = 1089.9$.

Pantheon+SH0ES

The Pantheon+SH0ES analysis represents an extension and refinement of the original Pantheon compilation. It includes 1701 light curves from 1550 Type Ia supernovae, collected across 18 surveys, with redshifts extending from 0.001 to 2.2613. A notable enhancement is the inclusion of 77 light curves from host galaxies with established Cepheid distances, which strengthens the calibration. Compared to the dataset presented by [49], Pantheon+SH0ES provides not only a broader sample, especially at low-redshift ($z < 0.01$), but also an extended redshift coverage. Furthermore, the analysis addresses several sources of systematic uncertainty, including those related to peculiar velocities, redshift determination, photometric calibration, and intrinsic scatter in SNe Ia. Unlike earlier studies, which treated the dark energy equation of state(EoS) and the Hubble constant(H_0) as independent variables, Pantheon+SH0ES acknowledges their interdependence, as both rely on overlapping supernova samples. Traditionally, H_0 estimates relied on nearby supernovae ($z < 0.01$) compared to those in the Hubble flow ($0.023 < z < 0.15$), while EoS constraints utilised supernovae up to $z \approx 2$, excluding the very low-redshift regime. Consequently, the 0.023–0.15 redshift interval has historically played a dual role, contributing to both H_0 and EoS determinations. Advances in SN Ia catalog calibration now provide stronger constraints on dark energy through its effect on cosmic expansion. The authors in the references [50, 51] used Bayesian methods to test scattering models and probe non-Gaussianity in Pantheon+ residuals.

The cosmological parameters are estimated through the minimization of the chi-square statistic,

$$\chi_{\text{SN}}^2 = \Delta \mathbf{D}^\top C_{\text{tot}}^{-1} \Delta \mathbf{D}, \quad (29)$$

where the residual vector $\Delta \mathbf{D}$ consists of the 1701 supernova distance modulus residuals, defined as $\Delta D_k = \mu_k - \mu_{\text{model}}(z_k)$ with μ_k denoting the observed distance modulus and $\mu_{\text{model}}(z_k)$ the model prediction at redshift(z_k) see in reference [52]. The total covariance matrix is expressed as $C_{\text{tot}} = C_{\text{stat}} + C_{\text{syst}}$, which accounts for both statistical and systematic uncertainties by combining their respective covariance contributions. The theoretical distance modulus is defined as

$$\mu_{\text{model}}(z; \Phi) = 25 + 5 \log_{10} \left(\frac{d_L(z; \Phi)}{1 \text{ Mpc}} \right), \quad (30)$$

where the luminosity distance is

$$d_L(z; \Phi) = (1+z) c \int_0^z \frac{dz'}{H(z'; \Phi)}, \quad (31)$$

with z , c and Φ denotes the redshift, speed of light and the set of cosmological parameters respectively. In supernova studies, the absolute magnitude M and the Hubble constant(H_0) are strongly correlated, preventing them from being independently constrained with supernova data alone. This issue is resolved in the SH0ES analysis, where Cepheid host-galaxy distances are used to calibrate the absolute magnitude ($M = -19.253$), thus providing a direct anchor for the cosmic distance scale and yielding a precise determination of H_0 . The residuals [52] are defined as

$$\Delta\mu'_k = \begin{cases} \mu_k - \mu_k^{\text{Cep}}, & \text{if } i \text{ corresponds to a Cepheid host galaxy,} \\ \mu_k - \mu_{\text{model}}(z_k; \Phi), & \text{otherwise,} \end{cases} \quad (32)$$

where μ_k^{Cep} represents the SH0ES Cepheid-based distance modulus. The total covariance matrix, which incorporates both the statistical and systematic uncertainties from the Pantheon+ dataset together with the Cepheid calibration uncertainties, is written as

$$C_{\text{tot}} = C_{\text{SN}}^{\text{stat}} + C_{\text{SN}}^{\text{syst}} + C_{\text{Cep}}^{\text{stat}} + C_{\text{Cep}}^{\text{syst}}. \quad (33)$$

Finally, the combined chi-square employed to constrain cosmological models with the Pantheon+SH0ES sample is expressed as

$$\chi_{\text{tot}}^2 = \Delta D^T C_{\text{tot}}^{-1} \Delta D, \quad (34)$$

where C_{tot} incorporates both statistical and systematic uncertainties from supernovae and Cepheid host calibrations. This approach consistently combines the relative distances from Pantheon+ supernovae with the absolute calibration from SH0ES Cepheid hosts in the cosmological analysis.

Observational Gravitational-Wave Catalogs (LIGO–Virgo–KAGRA)

Gravitational waves are ripples in the fabric of spacetime, first predicted by Albert Einstein's General Theory of Relativity (1916). They are produced when massive objects such as black holes or neutron stars undergo rapid acceleration, particularly during binary mergers, collisions, or asymmetric explosions like supernovae. These waves propagate at the speed of light and, owing to their weak interaction with matter, carry undistorted information about the most extreme astrophysical environments. The first direct detection, achieved on September 14, 2015, by the Advanced LIGO interferometers, confirmed general relativity in the strong-field regime and inaugurated the era of gravitational-wave astronomy [53] exactly after a century of Einstein prediction. Since then, the inclusion of the European Virgo detector [54] and the Japanese KAGRA observatory [55] into the global

network has significantly improved sky localization, detection confidence, and parameter estimation, thereby enabling multi-messenger astronomy and deepening our understanding of the dynamical universe.

In this study, we utilise observational data from the Gravitational-Wave Transient Catalogues (GWTC), a series of cumulative releases maintained by the LIGO–Virgo–KAGRA (LVK) Collaboration, which document compact binary coalescences across successive observing runs. The first release, GWTC-1, reported 11 confident detections from the O1 (2015–2016) and O2 (2016–2017) runs, including several binary black hole (BBH) mergers and the landmark binary neutron star (BNS) event GW170817 [56]. The subsequent catalog, GWTC-2, added 39 detections from the first half of O3 (O3a, April–October 2019), extending the sample to higher redshifts and asymmetric mass ratios [57]. A refined analysis of the same data, published as GWTC-2.1, identified 46 candidate events with improved calibration and parameter estimation [58]. The GWTC-3 catalog expanded the collection further by reporting 35 additional compact binary mergers from the second half of O3 (O3b, November 2019–March 2020), of which 17 were newly identified [59]. Complementary efforts, such as the IAS-O3a catalog, provided 42 BBH detections based on independent analysis, while auxiliary lists and marginal candidate sets offered further context. Most recently, early results from the O4 observing run have been released through discovery papers, and updated catalogs are expected to expand the current sample. Altogether, the GWTC series now contains 225 confirmed gravitational-wave detections, providing the most extensive observational record of compact binary coalescences. In this work, we utilize 90 gravitational-wave observational events, focusing on the luminosity distance (d_L) and the corresponding redshift measurements.

3.1 Results and discussion

The results of our cosmological model are discussed in this section by focusing on the behavior of the Hubble parameter $H(z)$. A direct comparison with observational data enables us to examine the validity of the model and to constrain the values of the key cosmological parameters. Figure 1 presents the 33 observational Hubble parameter data points with their respective error bars, together with the best-fit theoretical curve obtained via least-squares analysis. The model effectively reproduces the increasing trend of $H(z)$ with redshift, with most data points falling within the error bounds of the fit, demonstrating strong consistency between observations and theory. This visual agreement is supported by statistical diagnostics: the reduced chi-square value of 0.6 indicates an excellent fit without signs of overfitting. The model evaluation was carried out using the Akaike Information Criterion (AIC) and the Bayesian Information Criterion (BIC). These are expressed as $AIC = \chi_{\min}^2 + 2k$, $BIC = \chi_{\min}^2 + k \ln(N)$, where N is the sample size and k is the number of model parameters. For the present analysis, we obtain $AIC = -5.52$ and $BIC = 10.57$, which indicate a

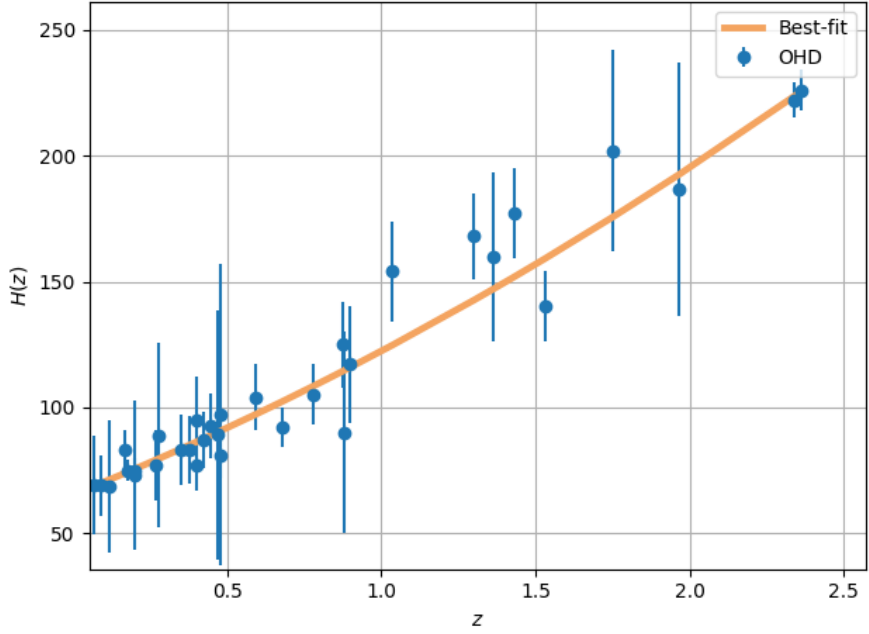


Figure 1: Hubble parameter measurements from OHD with best-fit cosmological model curve.

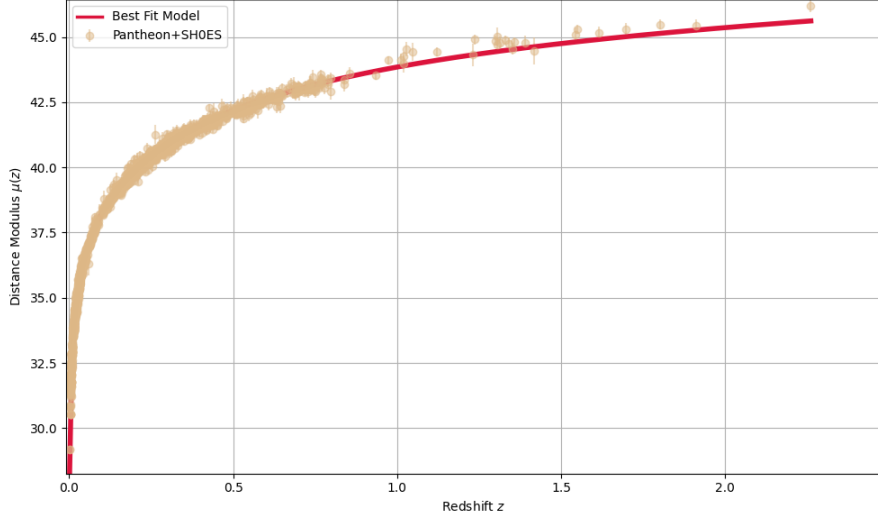


Figure 2: Distance modulus from Pantheon+SH0ES supernova data compared with the best-fit model curve

statistically preferred fit while avoiding unnecessary model complexity. Moreover, the coefficient of determination ($R^2 = 0.93$) confirms the robustness of the model, highlighting its reliability in describing the late-time expansion history of the universe. Figure 2 presents the distance modulus $\mu(z)$ of the 1701 Pantheon+SH0ES supernova dataset compared with the theoretical prediction from the best-fit cosmological model. The fitted curve successfully traces the observed trend, capturing both

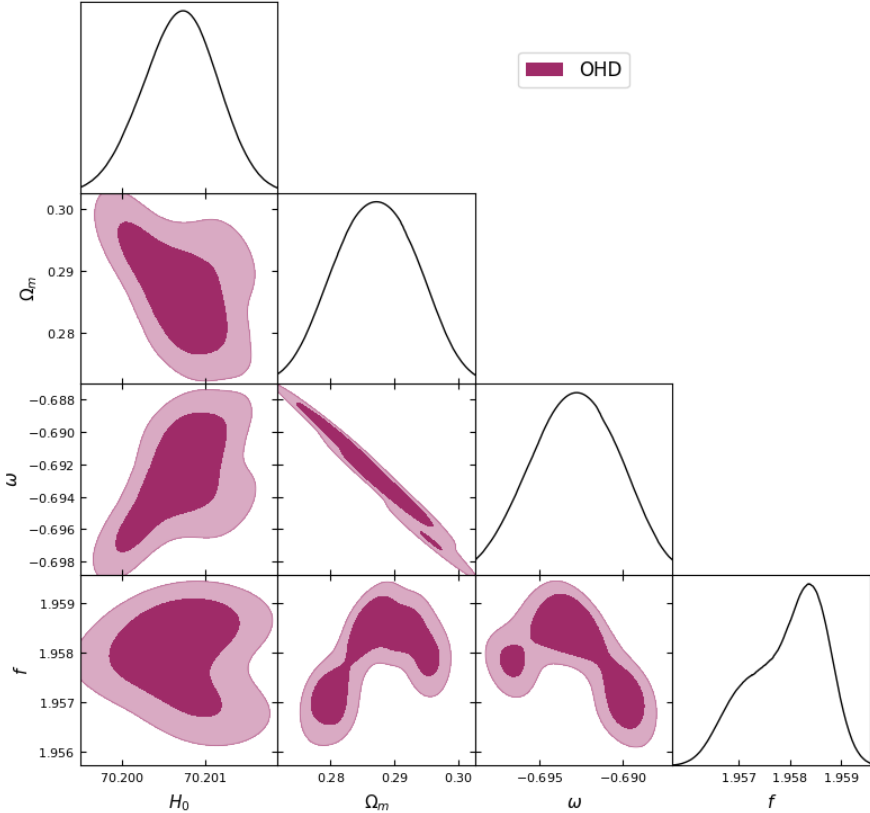


Figure 3: Posterior constraints on $(H_0, \Omega_m, \omega$ and $f)$ from OHD, with 1D marginalized distributions and 2D contours at 68% and 95% confidence levels.

the rapid rise of $\mu(z)$ at low redshift and its gradual flattening at higher z . The close overlap between the data points and the model demonstrates strong agreement across the full redshift range, with most observations lying well within the associated uncertainties. The quality of the fit is further quantified by statistical indicators. The χ^2 value of 2118.1741 with a reduced χ^2 of 1.03 confirms excellent consistency between the model and the data, without evidence of overfitting.

The results of the MCMC analysis are further illustrated in figures 3 to 7, which display the posterior distributions of the model parameters derived from different observational datasets, together with the comparisons between the observed data and the theoretical predictions of the best-fit cosmological model. The central solid line represents the best-fit curve obtained from parameter estimation, while the surrounding shaded regions mark the confidence levels. Specifically, the lighter shaded region represents the 68% confidence interval, while the darker region indicates the 95% confidence interval, both derived by propagating the uncertainties from the fitted parameters. These confidence bands highlight the robustness and consistency of the model fitting. Figure 3 shows that the one-dimensional posteriors are sharply peaked, reflecting strong constraints on the parameters. The two-dimensional contours highlight parameter correlations, with a clear degeneracy between the matter density param-

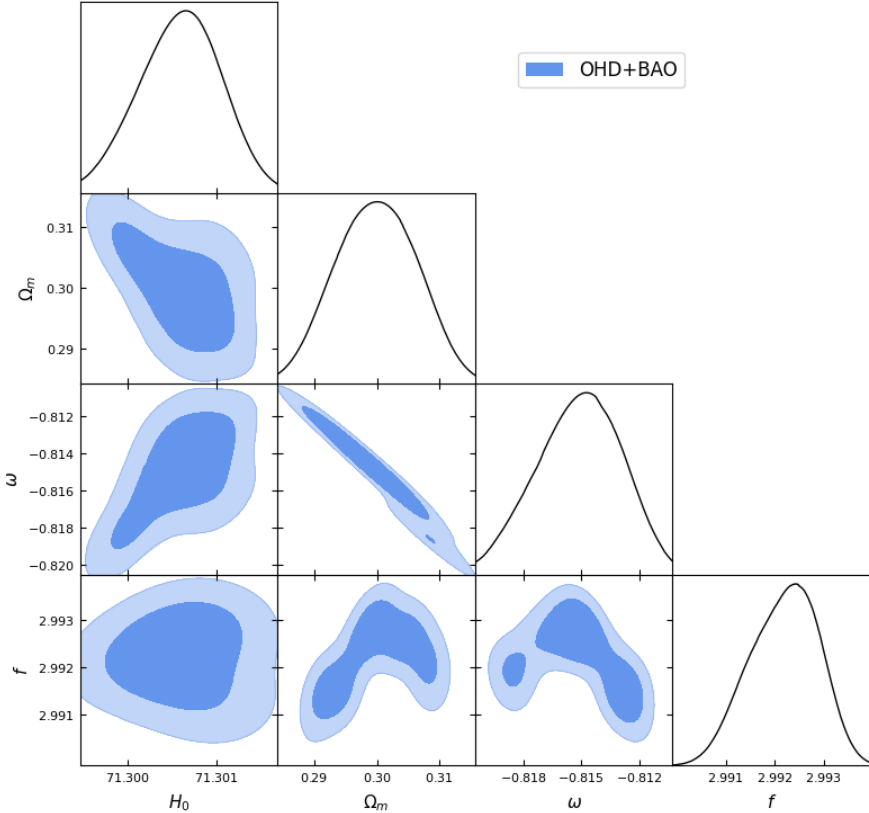


Figure 4: Posterior constraints on $(H_0, \Omega_m, \omega$ and $f)$ from OHD+BAO, with 1D marginalized distributions and 2D contours at 68% and 95% confidence levels.

eter and the equation of state parameter, while other parameters remain largely independent. Overall, the figure confirms that the OHD dataset provides robust and precise constraints within the considered cosmological framework. Figure 4 shows the results of the combined analysis using 33 OHD and 17 BAO measurements. The one-dimensional marginalised posteriors again exhibit narrow peaks, reflecting precise parameter determinations. The contour plots highlight correlations among parameters, especially between Ω_m and ω . Incorporating BAO data alongside OHD substantially sharpens the parameter constraints, reducing uncertainties and yielding tighter confidence regions. These results highlight the effectiveness of joint datasets in enhancing the accuracy and consistency of cosmological parameter estimation.

The joint analysis of OHD and CMB data, as shown in Figure 5, further sharpens the constraints on the cosmological parameters. The one-dimensional posterior distributions are highly peaked, confirming the precision of the estimates. The two-dimensional contours reveal that Ω_m and ω remain strongly correlated, while other parameters show weaker or negligible correlations. Compared with the OHD+BAO case, the inclusion of CMB data shifts the preferred value of the equation of state towards a more negative region and tightens the allowed range of the coupling parameter, thereby

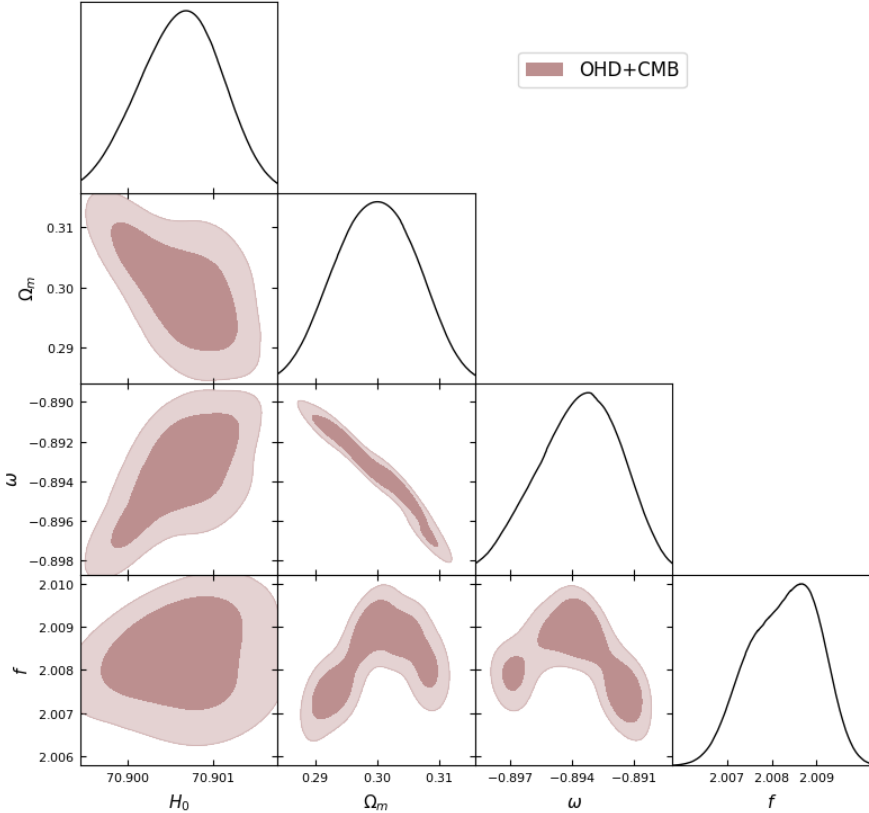


Figure 5: Posterior constraints on $(H_0, \Omega_m, \omega$ and $f)$ from OHD+CMB, with 1D marginalized distributions and 2D contours at 68% and 95% confidence levels.

reducing uncertainties. This demonstrates that combining CMB information with OHD significantly enhances the robustness of the analysis and provides more stringent bounds on the model parameters. Figure 6 shows the joint analysis of OHD, BAO, and CMB data, yielding very tight parameter constraints. The confidence regions are narrower than the two-dataset cases, with ω moving closer to the cosmological constant boundary. This highlights the complementarity of the three datasets in reducing degeneracies and improving precision. Figure 7 presents the results from the combined Pantheon supernova and SH0ES data. The posteriors are sharply peaked, showing that this dataset combination yields highly precise parameter constraints. The confidence regions are significantly narrower compared to the previous cases, reflecting the strong constraining power of the Pantheon sample together with the SH0ES calibration. The contours also reveal correlations among parameters, particularly between Ω_m and ω . Overall, this analysis points to a quintessence-like dark energy component and a slightly lower matter density compared with the OHD+BAO+CMB results. Using OHD, BAO, CMB, and Pantheon+SH0ES together leads to tighter and more consistent constraints than relying on a single observational probe. While the OHD+BAO+CMB combination drives the dark energy equation of state parameter ω close to the cosmological constant boundary, the Pan-

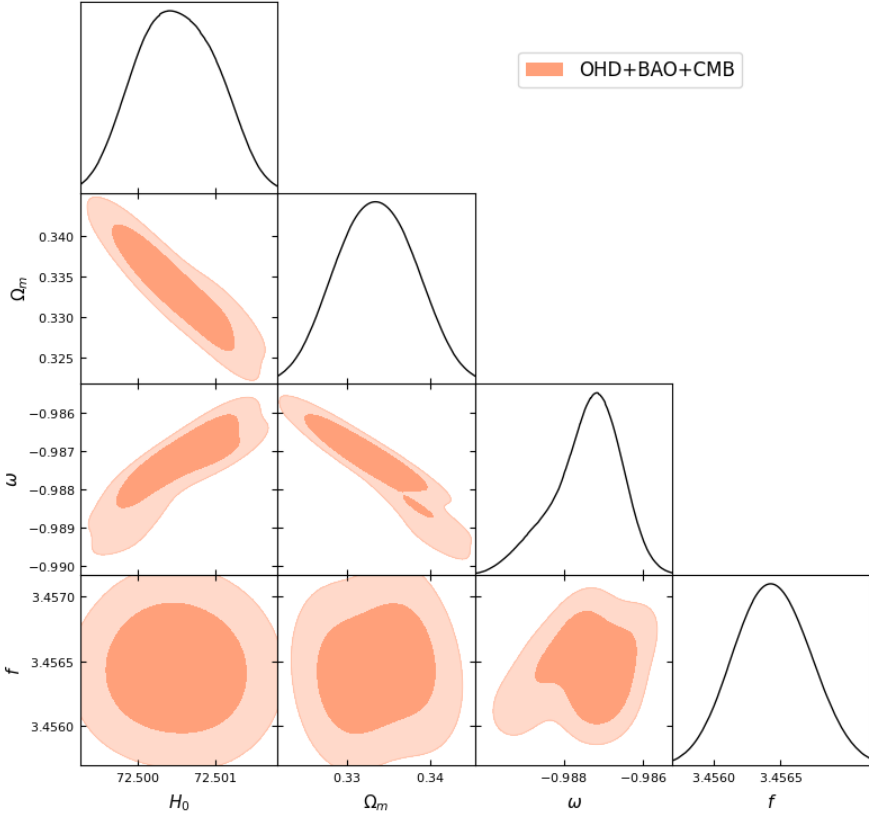


Figure 6: Posterior constraints on $(H_0, \Omega_m, \omega$ and $f)$ from OHD+BAO+CMB, with 1D marginalized distributions and 2D contours at 68% and 95% confidence levels.

theon+SH0ES data favour a quintessence-like behaviour with remarkably small uncertainties. These results demonstrate the power of combining multiple observational probes in reducing degeneracies and achieving highly precise cosmological parameter constraints. From a physical standpoint, the obtained parameter constraints imply that the present anisotropic $f(T)$ model provides a viable geometric mechanism for late-time cosmic acceleration. The equation-of-state parameter ω consistently lies within the quintessence regime ($-0.99 \lesssim \omega \lesssim -0.69$), indicating a dynamical rather than constant dark-energy behavior emerging from torsional effects. The matter density parameter Ω_m values are also in excellent agreement with observational bounds from the Λ CDM model, demonstrating that the inclusion of anisotropy does not conflict with current large-scale observations.

The variation of luminosity distance with redshift is displayed in figure 8, where the relation $d_L(z)$ is obtained from 90 gravitational-wave detections reported by the LIGO+Virgo+KAGRA collaboration. The orange points with error bars represent the luminosity distances measured for individual GW events, with the spread becoming larger at higher z due to increasing uncertainties. The solid green curve corresponds to the best-fit cosmological model prediction, which is consistent with the Λ CDM framework. This concordance demonstrates that gravitational-wave distance indicators provide inde-

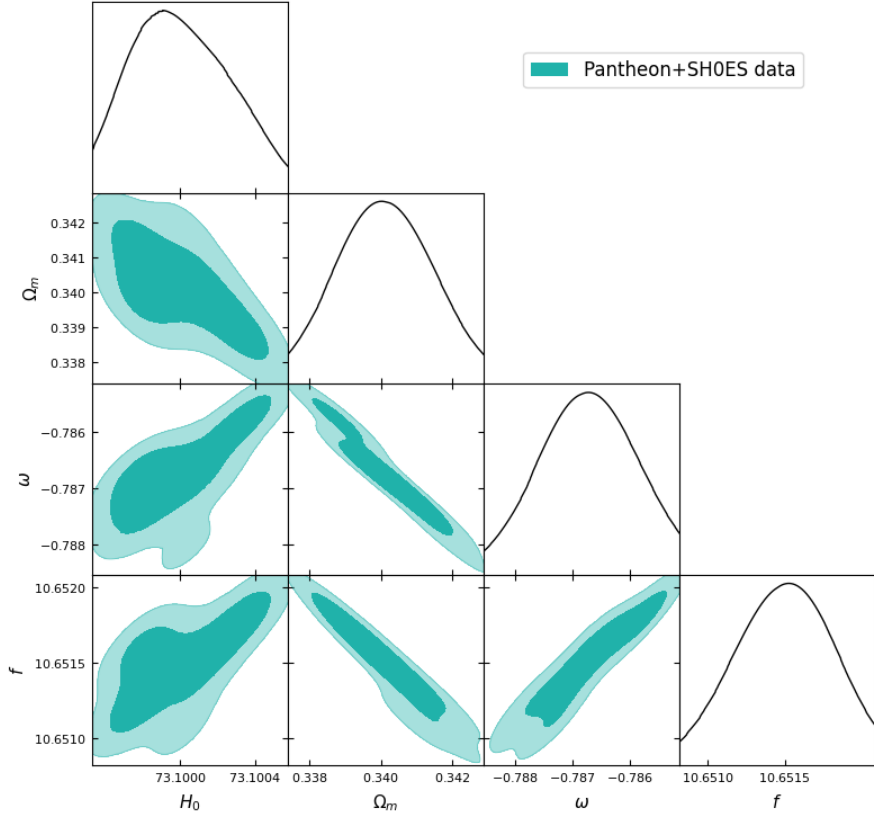


Figure 7: Posterior constraints on $(H_0, \Omega_m, \omega$ and $f)$ from Pantheon+SH0ES, with 1D marginalized distributions and 2D contours at 68% and 95% confidence levels.

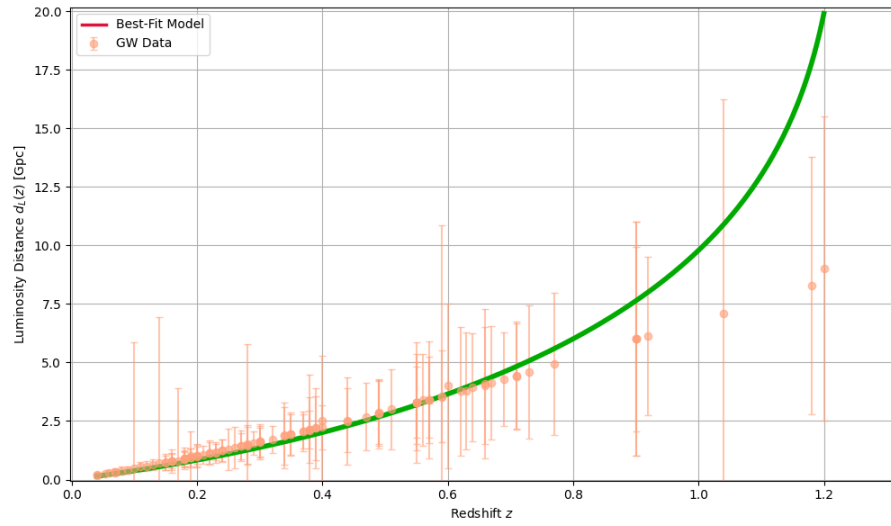


Figure 8: Comparison of redshift–luminosity distance relation from GW data and theoretical fit.

pendent distance measurements, complementing conventional probes and offering a promising avenue

to address the current Hubble constant tension.

4 Conclusion

The universe has been undergoing continuous expansion since the Big Bang, with galaxies receding from one another as the fabric of space itself stretches. Observational evidence, particularly from supernova surveys, reveals that this expansion is not merely persisting but accelerating. The driving agent behind this phenomenon is termed dark energy, an enigmatic component constituting nearly 70% of the cosmic energy budget. Acting as a repulsive force counter to gravity, dark energy propels the accelerated growth of the universe and remains one of the greatest mysteries in modern cosmology [60]. In order to understand this cosmic acceleration, scientists have also proposed modified theories of gravity, such as $f(T)$ gravity. Unlike General Relativity, which is based on spacetime curvature, $f(T)$ gravity employs the torsion scalar T . By extending it to a general function $f(T)$, the theory can explain the universe's accelerated expansion without explicitly invoking dark energy, offering an alternative perspective on cosmic dynamics. The key novelty of the present work lies in the construction of a plane-symmetric anisotropic cosmological model in exponential $f(T)$ gravity, where the Hubble function $H(z)$ emerges self-consistently from the field equations rather than being imposed externally. This provides a direct theoretical link between the geometry and cosmic expansion dynamics, distinguishing the model from previously studied isotropic $f(T)$ and Λ CDM frameworks. Motivated by these considerations, we adopt this geometric setup to explore the dynamical behavior of the universe under the exponential form $f(T) = T + ue^{-vT}$, which is known to provide rich cosmological implications and can be confronted with various observational data sets such as SH0ES, baryon acoustic oscillations (BAO), cosmic microwave background (CMB), and Hubble parameter measurements.

The Hubble parameter (H) arises naturally from the constructed model, playing a central role in describing the expansion dynamics and confronting the theory with observations [61]. From Figure 1, it is evident that the best-fit $H(z)$ curve shows strong statistical agreement with the observational Hubble data (OHD), remaining within the error margins across most redshifts. This demonstrates the effectiveness of the present plane-symmetric anisotropic $f(T)$ model with $f(T) = T + ue^{-vT}$ in reproducing the observed expansion history of the universe. Figure 2 demonstrates that the best-fit distance modulus curve closely follows the Pantheon+SH0ES supernova data, indicating that this anisotropic $f(T)$ model successfully accounts for late-time cosmic acceleration.

From figures 3 to 7, the value of the Hubble constant H_0 varies depending on the choice of observational data set and measurement techniques. Early-universe probes such as the Planck CMB data yield a lower value around $67\text{--}68 \text{ km s}^{-1}\text{Mpc}^{-1}$, whereas local distance-ladder measurements from the SH0ES collaboration give a higher value of about $73\text{--}74 \text{ km s}^{-1}\text{Mpc}^{-1}$. Intermediate es-

timates are obtained from Tip of the Red Giant Branch (TRGB) calibration and megamaser-based geometric methods, which suggest values near $69\text{--}71 \text{ km s}^{-1}\text{Mpc}^{-1}$. Combined analyses involving BAO and supernova data also converge close to $70 \text{ km s}^{-1}\text{Mpc}^{-1}$. Overall, considering different data sets, the Hubble constant lies roughly in the range $65 \lesssim H_0 \lesssim 75 \text{ km s}^{-1}\text{Mpc}^{-1}$. In the present analysis, we constrained the Hubble parameter H_0 using several observational data sets within the framework of this plane-symmetric anisotropic $f(T)$ cosmological model with the functional form $f(T) = T + ue^{-vT}$. Using OHD data alone, we obtain a tightly peaked value around $H_0 \approx 70.2 \text{ km s}^{-1}\text{Mpc}^{-1}$. Incorporating the recent DESI BAO measurements shifts the estimate to $H_0 \approx 71.3 \text{ km s}^{-1}\text{Mpc}^{-1}$, while the OHD+CMB combination yields $H_0 \approx 70.9 \text{ km s}^{-1}\text{Mpc}^{-1}$. The Pantheon+SH0ES sample favors a slightly higher value near $H_0 \approx 73.1 \text{ km s}^{-1}\text{Mpc}^{-1}$, and the joint OHD+DESI BAO+CMB analysis provides $H_0 \approx 72.5 \text{ km s}^{-1}\text{Mpc}^{-1}$. Thus, our results remain consistent with the global observational bounds and constrain the Hubble constant to the range $70 \lesssim H_0 \lesssim 73 \text{ km s}^{-1}\text{Mpc}^{-1}$, which is in good agreement with late-time cosmological measurements. Notably, the model yields intermediate H_0 values that naturally reconcile early- and late-time measurements, suggesting a potential geometric pathway toward alleviating the Hubble tension.

The matter density parameter Ω_m was also constrained using different combinations of data sets within this anisotropic $f(T)$ model. The OHD data alone prefer a value of $\Omega_m \approx 0.28$, while the inclusion of DESI BAO measurements increases the estimate to $\Omega_m \approx 0.29\text{--}0.31$. A joint analysis of OHD and CMB data yields a similar result around $\Omega_m \approx 0.30$, which is consistent with standard cosmology. The Pantheon+SH0ES compilation favors a slightly higher value, $\Omega_m \approx 0.34$, and the combined OHD+DESI BAO+CMB analysis provides $\Omega_m \approx 0.33$. Overall, this analysis places the matter density parameter in the range $0.28 \lesssim \Omega_m \lesssim 0.34$, and is perfectly consistent with observational constraints from other cosmological probes.

Alongside the matter density parameter, it is equally important to constrain the equation-of-state (EoS) parameter ω , as it governs the dynamical behavior of cosmic acceleration. Using OHD data alone, we find $\omega \approx -0.695$, while the inclusion of DESI BAO shifts the value to $\omega \approx -0.818$. A joint analysis with OHD+CMB data yields a tighter constraint at $\omega \approx -0.894$. The Pantheon+SH0ES sample provides $\omega \approx -0.787$, and the combined OHD+DESI BAO+CMB analysis favors a value close to $\omega \approx -0.987$. Overall, our analysis places the EoS parameter in the range $-0.99 \lesssim \omega \lesssim -0.69$, which consistently lies in the quintessence region and approaches the cosmological constant limit.

From a physical perspective, the present analysis demonstrates that the late-time acceleration of the universe can emerge naturally from torsional effects in spacetime geometry, without invoking an explicit dark-energy component. The exponential form of $f(T)$ effectively mimics a dynamic dark-energy behavior, driving the observed acceleration while remaining consistent with current cosmological constraints. This result indicates that cosmic acceleration may have a purely geometric origin, arising from the intrinsic properties of spacetime rather than an external energy source.

From figure 8, the best-fit luminosity distance $d_L(z)$ curve shows a good agreement with the available GW data, lying within the observational uncertainties across the redshift range. This indicates that our anisotropic $f(T)$ model can successfully reproduce the distance–redshift relation for gravitational-wave sources, thereby providing an independent validation of the model against GW observations.

Theoretically, the results obtained here strengthen the position of torsion-based modified gravity as a viable geometric alternative to curvature-based theories such as $f(R)$ and scalar-tensor models. The emergence of late-time acceleration from torsional effects suggests that cosmic dynamics may fundamentally depend on the choice of spacetime connection, offering new perspectives on the unification of gravity and cosmology. Overall, our study demonstrates that the anisotropic $f(T)$ model with the chosen exponential functional form provides a consistent and robust description of the late-time accelerated expansion of the universe, offering an alternative perspective on cosmic dynamics without invoking an explicit dark-energy component. In future work, one may extend this study by exploring alternative functional forms of $f(T)$, as well as other anisotropic space-time geometries such as Bianchi or Kantowski–Sachs model. Incorporating forthcoming high-precision data sets from DESI, Euclid, LSST, and next-generation gravitational-wave observatories will allow for tighter parameter constraints. Furthermore, examining perturbation dynamics, structure formation, and thermodynamical aspects of the model could provide deeper insights into the role of torsion in cosmic evolution.

5 Acknowledgement

We gratefully acknowledge the use of data and resources provided by the Dark Energy Spectroscopic Instrument (DESI) collaboration. DESI is managed by the U.S. Department of Energy’s Office of Science and is supported by a collaboration of universities and laboratories worldwide. We also acknowledge the contributions of the Gravitational Wave Science Collaboration (GWSCO), whose efforts in advancing gravitational-wave detection and analysis have been invaluable to this work. Dr. T. Vinutha acknowledges the Inter-University Centre for Astronomy and Astrophysics (IUCAA), Pune, for providing research facilities and support under the Visiting Associateship Programme.

References

- [1] A. G. Riess *et al.*, Astron. J. **116**, 1009(1998)
- [2] S. Perlmutter *et al.*, Astrophys. J. **517**, 565(1999)
- [3] Y. F. Cai, S. Capozziello, M. De Laurentis, E. N. Saridakis, Rep. Prog. Phys. **79**, 106901(2016)

- [4] B. Mirza, F. Oboudiat, *JCAP* **11**, 011(2017)
- [5] C. Q. Geng, C. C. Lee, E. N. Saridakis, Y. P. Wu, *Phys. Lett. B* **704**, 384(2011)
- [6] G. Otalora, *Phys. Rev. D* **88**, 063505(2013)
- [7] S. Bahamonde, S. Capozziello, M. Faizal, R. Myrzakulov, *Eur. Phys. J. C* **75**, 289(2015)
- [8] J. B. Dent, S. Dutta, E. N. Saridakis, *JCAP* **01**, 009(2011)
- [9] F. B. M. dos Santos, J. E. Gonzalez, R. Silva, *Eur. Phys. J. C* **82**, 107(2022)
- [10] M. Koussour, A. Altaibayeva, S. Bekov, F. Holmurodov, S. Muminov, J. Rayimbaev, *Phys. Dark Univ.* **46**, 101664(2024)
- [11] X. Jiang, X. Ren, Z. Li, Y. F. Cai, X. Er, *Mon. Not. Roy. Astron. Soc.* **528**, 1965(2024)
- [12] Y. Xie, X. M. Deng, *Mon. Not. Roy. Astron. Soc.* **433(4)**, 3584(2013)
- [13] N. Dimakis, A. Paliathanasi, T. Christodoulakis, *Phys. Rev. D* **109**, 024031(2024)
- [14] M. Ghosh, C. Aktaş, S. Chattopadhyay, *Eur. Phys. J. C* **85**, 727(2025)
- [15] A. Golovnev, T. Koivisto, M. Sandstad, *Phys Lett. B.* **810**, 135840(2020)
- [16] A. Paliathanasis, *Math. Methods Appl. Sci.* **46 (11)**, 12087(2023)
- [17] N. Secret, S. von Hausegger, M. Rameez, R. Mohayaee, S. Sarkar, J. Colin, *Astrophys. J. Lett.* **908**, L51(2021)
- [18] O. Akarsu, S. Kumar, S. Sharma, L. Tedesco, *Phys. Rev. D* **100**, 023532(2019)
- [19] T. Vinutha, K. S. Kavya, K. Niharika, *Phys. Dark Universe* **34**, 100896(2021)
- [20] T. Vinutha, K. S. Kavya, *Eur. Phys. J. Plus* **135**, 306(2020)
- [21] T. Koivisto, D. F. Mota, *JCAP* **06**, 018(2008)
- [22] B. Saha, *Phys. Rev. D* **74**, 124030(2006)
- [23] M. E. Rodrigues, M. J. S. Houndjo, D. Saez-Gomez, F. Rahaman, *Phys. Rev. D* **86**, 104059(2012)
- [24] B. Mishra, *Chin. Phys. Lett.* **21**, 2359(2004)
- [25] Y. Adityaa, U.Y. Divya Prasanthi, D.R.K. Reddy, *New Astronomy* **84**, 101504(2021)

[26] M. F. Shamir, A. Saeed, *Theor. Math. Phys.* **197**, 1845(2018)

[27] V. U. M. Rao, T. Vinutha, *Astrophys. Space Sci* **325**, 59(2010)

[28] K. S. Thorne, *Astrophys J* **148**, 51(1967)

[29] R. Kantowski, R. K. J. Sachs, *Math Phys.* **7**, 433(1966)

[30] J. Kristian, R. K. Sachs, *Astrophys J* **143**, 379(1966)

[31] C. B. Collins, E. N. Glass, D. A. Wilkinson , *Gen. Relativ. Gravit* **12**, 805(1980)

[32] O. Akarsu, C. B. Kilinc, *Gen. Rel. Grav.* **42**, 763 (2010)

[33] M. Sharif, M. Zubair, *Astrophys. Space Sci.* **330**, 399(2010)

[34] U. Y. Divya Prasanthi, Y. Aditya, *Phys. Dark Univ.* **31**, 100782(2021)

[35] R. Jimenez, L. Verde, T. Treu, D. Stern, *ApJ* **593**, 622(2003)

[36] D. Stern, R. Jimenez, L. Verde, M. Kamionkowski, S. A. Stanford, *JCAP* **02**, 008(2010)

[37] M. Moresco *et al.*, *J. Cosmol. Astropart. Phys.* **08**, 006(2012)

[38] C. Zhang, H. Zhang, S. Yuan, S. Liu, T. J. Zhang, Y.C. Sun, *Res. Astron. Astrophys.* **14**, 1221(2014)

[39] A. L. Ratsimbazafy, S. I. Loubser, S.M. Crawford, C. M. Cress, B. A. Bassett, R. C. Nichol, P. Väisänen, *Mon. Not. R. Astron. Soc.* **467**, 3239(2017)

[40] M. Moresco, R. Jimenez, L. Verde, A. Cimatti, L. Pozzetti, *ApJ* **898**, 82(2020)

[41] T. Delubac *et al.*, *Astron. Astrophys.* **574**, A59(2015)

[42] A. G. Adame *et al.*, *AJ* **168**, 58(2024)

[43] F. Beutler, C. Blake, M. Colless, D. H. Jones, L. Staveley- Smith, L. Campbell, Q. Parker, W. Saunders, F. Watson, *Mon. Not. R. Astron. Soc.* **416**, 3017(2011)

[44] A. J. Ross, L. Samushia, C. Howlett, W. J. Percival, A. Burden, M. Manera, *Mon. Not. R. Astron. Soc.* **449**, 835(2015)

[45] N. Padmanabhan, X. Xu, D. J. Eisenstein, R. Scalzo, A. J. Cuesta, K. T. Mehta, E. Kazin, *Mon. Not. R. Astron. Soc.* **427**, 2132(2012)

[46] L. Anderson *et al.*, Mon. Not. R. Astron. Soc. **441**, 24 (2014)

[47] C. Blake *et al.*, Mon. Not. R. Astron. Soc. **425**, 405(2012)

[48] P. A. R. Ade *et al.*, Astron. Astrophys. **594**, A13(2016)

[49] D. M. Scolnic *et al.*, ApJ **859**, 101(2018)

[50] T. Lovick, S. Dhawan, W. Handley, Mon. Not. R. Astron. Soc. **536**, 234(2025)

[51] M. G. Dainotti, G. Bargiacchi, M. Bogdan, S. Capozziello, S. Nagataki, JHEAP **41**, 30(2024)

[52] S. S. Mishra , N. S. Kavya , P. K. Sahoo , V. Venkatesha, AJ **981**, 13(2025)

[53] B. P. Abbott *et al.*, Phys. Rev. Lett. **116(6)**, 061102(2016)

[54] F. Acernese *et al.*, Class. Quantum Gravity **32(2)**, 024001(2015)

[55] T. Akutsu *et al.*, Progress of Theoretical and Experimental Physics **2021(5)**, 05A101(2021)

[56] B. P. Abbott *et al.*, Phys. Rev. X **9**, 031040(2019)

[57] R. Abbott *et al.*, Phys. Rev. X **11**, 021053(2021)

[58] R. Abbott *et al.*, Phys. Rev. D **11**, 022001(2024)

[59] R. Abbott *et al.*, Phys. Rev. X **13**, 041039(2023)

[60] L. Amendola, S. Tsujikawa, Cambridge University Press, (2015)

[61] E. D. Valentino, A. Melchiorri, O. Mena, S. Vagnozzi, Phys. Dark Univ. **30**, 100666(2020)

6 Appendix

$$\begin{aligned}\kappa_1 &= \frac{(-0.015625)(\iota+2)^7(5\iota+3)(-18.84955592)}{(3\iota+2)(2\iota+1)^2\iota^5c^7\alpha_0^7}, \\ \kappa_2 &= \frac{\frac{1}{32}(\iota+2)^7(-18.84955592)}{(3\iota+2)(2\iota+1)\iota^5c^7\alpha_0^7}, \\ \kappa_3 &= \left(\frac{-0.03125(\iota+2)^7(1-c_1(\iota+2))}{\iota^5c^7\alpha_0^7(3\iota+2)^2} \right) (-18.84955592), \\ \kappa_4 &= \mathcal{A}_0 + \mathcal{A}_1 + \mathcal{A}_4,\end{aligned}$$

where,

$$\begin{aligned}
\mathcal{A}_0 &= \left(\frac{-0.03125 (\iota + 2)^7 (1 - c_1(\iota + 2))}{\iota^5 c^7 \alpha_0^7 (3\iota + 2)^2} \right) \\
&\quad \left\{ \frac{1}{(\iota + 2)^2} \left(0.125 l(\iota + 2)^2 \exp \left[\frac{2\iota c^2 \alpha_0 v (3l + 2) \exp \left(\frac{-2\iota \ln(-c_1\iota - 2c_1 + 1)}{\iota + 2} \right)}{(\iota + 2)^2} \right] \right. \right. \\
&\quad \left. \left. - 6\alpha_0^2 c^2 \iota \left(l + \frac{2}{3} \right) \exp \left(\frac{-2\iota \ln(-c_1\iota - 2c_1 + 1)}{\iota + 2} \right) \right) \right. \\
&\quad \left. + \frac{0.0416 (\iota + 2)^2 \exp \left(\frac{2 \ln(-c_1\iota - 2c_1 + 1)}{\iota + 2} \right) (2\iota^2 + 3\iota + 1)}{\iota^3 c^2 \alpha_0^2 (3\iota + 2)} \right. \\
&\quad \left. - \frac{10.66666667 \alpha_0^8 c^8 \iota^6 (3\iota + 2)^2}{(\iota + 2)^8 (1 - c_1(\iota + 2))} \right\} \\
\mathcal{A}_1 &= \frac{-\frac{1}{32} (\iota + 2)^7 (1 - c_1(\iota + 2)) \mathcal{A}_2}{\iota^5 c^7 \alpha_0^7 (3\iota + 2)^2} + \frac{\frac{1}{32} (\iota + 2)^7 \mathcal{A}_3}{(3\iota + 2)(2\iota + 1) \iota^5 c^7 \alpha_0^7}, \\
\mathcal{A}_2 &= \frac{1}{8(\iota + 2)(2\iota + 1)(c_1\iota + 2c_1 - 1)} \left(-4l \exp \left(\frac{2\iota c^2 \alpha_0 v (3l + 2) \exp \left(\frac{-2\iota \ln(-c_1\iota - 2c_1 + 1)}{\iota + 2} \right)}{(\iota + 2)^2} \right) \right) \\
&\quad + \frac{1}{8} \left(\frac{12\alpha_0^2 c^2 \iota^2 \left(l + \frac{2}{3} \right) \exp \left(\frac{-2\iota \ln(-c_1\iota - 2c_1 + 1)}{\iota + 2} \right) (3\iota + 2)}{(\iota + 2)(2\iota + 1)(c_1\iota + 2c_1 - 1)} \right) \\
&\quad + \frac{0.0832 (\iota + 2) \exp \left(\frac{2 \ln(-c_1\iota - 2c_1 + 1)}{\iota + 2} \right) (2\iota^2 + 3\iota + 1)}{(2\iota + 1)(c_1\iota + 2c_1 - 1) \iota^3 c^2 \alpha_0^2} \\
&\quad + \frac{10.66666667 \alpha_0^8 c^8 \iota^6 (3\iota + 2)^3}{(\iota + 2)^8 (c_1\iota + 2c_1 - 1)(2\iota + 1)(1 - c_1(\iota + 2))}.
\end{aligned}$$

$$\begin{aligned}
\mathcal{A}_3 = & \frac{1}{8} \left(\frac{l(\iota+2)^2 \exp\left(\frac{2\iota c^2 \alpha_0 v (3l+2) \exp\left(\frac{-2\iota \ln(-c_1\iota - 2c_1 + 1)}{\iota+2}\right)}{(\iota+2)^2}\right)}{(\iota+2)^2} \right) \\
& - \frac{1}{8} \left(\frac{6\alpha_0^2 c^2 \iota \left(l + \frac{2}{3}\right) \exp\left(\frac{-2\iota \ln(-c_1\iota - 2c_1 + 1)}{\iota+2}\right)}{(\iota+2)^2} \right) \\
& - + \frac{0.0416 (\iota+2)^2 \exp\left(\frac{2 \ln(-c_1\iota - 2c_1 + 1)}{\iota+2}\right) (2\iota^2 + 3\iota + 1)}{\iota^3 c^2 \alpha_0^2 (3\iota+2)} \\
& - \frac{10.66666667 \alpha_0^8 c^8 \iota^6 (3\iota+2)^2}{(\iota+2)^8 (1 - c_1(\iota+2))}.
\end{aligned}$$

$$\begin{aligned}
\mathcal{A}_4 = & \frac{(-0.03125) (\iota+2)^7 (1 - c_1(\iota+2)) \mathcal{A}_5}{\iota^5 c^7 \alpha_0^7 (3\iota+2)^2} + \frac{0.03125 (\iota+2)^7 \mathcal{A}_7}{(3\iota+2)(2\iota+1) \iota^5 c^7 \alpha_0^7} \\
& + \frac{(-0.015625) (\iota+2)^7 (5\iota+3) \mathcal{A}_8}{(3\iota+2)(2\iota+1)^2 \iota^5 c^7 \alpha_0^7},
\end{aligned}$$

$$\begin{aligned}
\mathcal{A}_5 = & \frac{0.125 (2l) \exp\left(\frac{2\iota c^2 \alpha_0 v (3l+2) \exp\left(\frac{-2\iota \ln(-c_1\iota - 2c_1 + 1)}{\iota+2}\right)}{(\iota+2)^2}\right) \iota^2 c^2 \alpha_0 v (3l+2) (3\iota+2) \mathcal{A}_6}{(\iota+2)^4 (2\iota+1)^2 (c_1\iota + 2c_1 - 1)^2} \\
& + \frac{(-6) \alpha_0^2 c^2 \iota^2 \left(l + \frac{2}{3}\right) \exp\left(\frac{-2\iota \ln(-c_1\iota - 2c_1 + 1)}{\iota+2}\right) (5\iota^3 c_1 + 23\iota^2 c_1 + 32c_1\iota + 4\iota^2 + 12c_1 - \iota - 2)}{(\iota+2)^2 (2\iota+1)^2 (c_1\iota + 2c_1 - 1)^2} \\
& + \frac{(-0.0416) \exp\left(\frac{2 \ln(-c_1\iota - 2c_1 + 1)}{\iota+2}\right) (5\iota^3 c_1 + 23\iota^2 c_1 + 32c_1\iota - 2\iota^2 + 12c_1 - 11\iota - 6)}{(2\iota+1)^2 (c_1\iota + 2c_1 - 1)^2 \iota^3 c^2 \alpha_0^2} \\
& + \frac{(-10.66666667) \left(\frac{0.5 \alpha_0^8 c^8 \iota^6 (3\iota+2) (5\iota+3)}{(\iota+2)^8 (c_1\iota + 2c_1 - 1) (2\iota+1)^2} + \frac{\alpha_0^8 c^8 \iota^6 (3\iota+2)^2}{(\iota+2)^8 (c_1\iota + 2c_1 - 1)^2 (2\iota+1)^2} \right) (3\iota+2)^2}{1 - c_1(\iota+2)}
\end{aligned}$$

$$\mathcal{A}_6 = 36 \exp\left(\frac{-2\iota \ln(-c_1\iota - 2c_1 + 1)}{\iota+2}\right) \alpha_0 c^2 \iota^3 l v + 24 \exp\left(\frac{-2\iota \ln(-c_1\iota - 2c_1 + 1)}{\iota+2}\right) \alpha_0 c^2 \iota^3 v$$

$$\begin{aligned}
& + 24 \exp\left(\frac{-2\iota \ln(-c_1\iota - 2c_1 + 1)}{\iota + 2}\right) \alpha_0 c^2 \iota^2 l v + 16 \iota^2 c^2 \alpha_0 v \exp\left(\frac{-2\iota \ln(-c_1\iota - 2c_1 + 1)}{\iota + 2}\right) \\
& + 5\iota^5 c_1 + 43\iota^4 c_1 + 144\iota^3 c_1 + 4\iota^4 + 232\iota^2 c_1 + 15\iota^3 + 176c_1\iota + 10\iota^2 + 48c_1 - 12\iota - 8.
\end{aligned}$$

$$\begin{aligned}
\mathcal{A}_7 = & \frac{0.125}{(\iota + 2)^2} \left(\frac{-4l \exp\left(\frac{2\iota c^2 \alpha_0 v (3l + 2) \exp\left(\frac{-2\iota \ln(-c_1\iota - 2c_1 + 1)}{\iota + 2}\right)}{(\iota + 2)^2}\right) \iota^2 c^2 \alpha_0 v (3l + 2) (3\iota + 2)}{(\iota + 2) (2\iota + 1) (c_1\iota + 2c_1 - 1)} \right. \\
& \left. + \frac{12 \alpha_0^2 c^2 \iota^2 \left(l + \frac{2}{3}\right) \exp\left(\frac{-2\iota \ln(-c_1\iota - 2c_1 + 1)}{\iota + 2}\right) (3\iota + 2)}{(\iota + 2) (2\iota + 1) (c_1\iota + 2c_1 - 1)} \right) \\
& + \frac{0.0832 (\iota + 2) \exp\left(\frac{2 \ln(-c_1\iota - 2c_1 + 1)}{\iota + 2}\right) (2\iota^2 + 3\iota + 1)}{(2\iota + 1) (c_1\iota + 2c_1 - 1) \iota^3 c^2 \alpha_0^2} \\
& + \frac{10.66666667 \alpha_0^8 c^8 \iota^6 (3\iota + 2)^3}{(\iota + 2)^8 (c_1\iota + 2c_1 - 1) (2\iota + 1) (1 - c_1(\iota + 2))}.
\end{aligned}$$

$$\begin{aligned}
\mathcal{A}_8 = & \frac{0.125}{(\iota + 2)^2} \left(l (\iota + 2)^2 \exp\left(\frac{2\iota c^2 \alpha_0 v (3l + 2) \exp\left(\frac{-2\iota \ln(-c_1\iota - 2c_1 + 1)}{\iota + 2}\right)}{(\iota + 2)^2}\right) - 6 \alpha_0^2 c^2 \iota \left(l + \frac{2}{3}\right) \right) \\
& + \frac{0.0416 (\iota + 2)^2 \exp\left(\frac{2 \ln(-c_1\iota - 2c_1 + 1)}{\iota + 2}\right) (2\iota^2 + 3\iota + 1)}{\iota^3 c^2 \alpha_0^2 (3\iota + 2)} \\
& - \frac{10.66666667 \alpha_0^8 c^8 \iota^6 (3\iota + 2)^2}{(\iota + 2)^8 (1 - c_1(\iota + 2))}.
\end{aligned}$$